Airglow monitoring by one-pixel detector

Š. Mackovjak [a],[*], P. Bobík [a], J. Baláž [a], I. Strhárský [a], M. Putiš [a], P. Gorodetzky [b]

[a] *Department of Space Physics, Institute of Experimental Physics, Slovak Academy of Sciences, Watsonova 47, 04001 Košice, Slovak Republic*
[b] *AstroParticle and Cosmology Laboratory, University Paris Diderot/CNRS–IN2P3, 10 rue A. Domon et L. Duquet, 75013 Paris, France*

ARTICLE INFO

ABSTRACT

The night time airglow is a dynamic phenomenon that acts as a background for the detection of the extensive air shower (EAS) fluorescence. It is a mandatory task to monitor this background for the ground-based telescopes and for the planned space-based telescopes, dedicated to observe the EAS events induced by the ultra-high energy cosmic rays. To perform this task, we have developed a one-pixel Airglow MONitor (AMON) instrument. This instrument provides the absolute intensities of the measured night sky background in the near-ultraviolet spectral range and in the one second temporal resolution. It is designed to be easily operated in different locations and so to offer required spatial resolution. The first results demonstrate that AMON data might be useful not only for the high-energy astrophysics purposes, but also for the studies of the airglow dynamics.

1. Introduction

The upper atmosphere of the Earth is continuously influenced by the solar radiation with short wavelengths. The processes, such as the ionization and dissociation of atmospheric atoms and molecules are followed by recombination and photochemical reactions, that lead to the production of a faint light commonly known as an airglow [1–3]. The airglow can be effectively observed by ground-based detectors during the night time, when the direct sunlight is absent [4,5]. Such measurements are important for the characterization and understanding of the airglow intensity variations, that depends on the geographical position, time, solar cycle, geomagnetic activity, and changes in the Earth's atmosphere [6,7]. The role of the airglow measurements has become important also for the high energy astrophysics from the last decades. The night airglow light with contribution of the starlight and the zodiacal light works as a diffuse night sky background (NSB) for detection of the extensive air shower (EAS) events. The estimation of absolute intensity of this background is essential for energy evaluation of EAS events with low statistics, i.e., events induced by interactions of ultra-high energy cosmic rays (UHECR) or very high energy (VHE) gamma rays in the Earth's atmosphere [8,9].

The EAS fluorescence light is produced when the nitrogen molecules (N_2) are excited by the interaction with the EAS secondary particles, and the following spontaneous de-excitation generates photons with characteristic wavelengths within 290–430 nm range [10]. Looking from the ground, the NSB for these events is composed mainly by the molecular oxygen (O_2) airglow radiation that is generated by the following process. The molecules of O_2 are dissociated by the solar short wavelength radiation during the day. During the night, the atoms

of oxygen (O) are recombined to oxygen excited molecules (O_2^*). The molecules in the metastable state have a short lifetime, therefore the recombination is followed by the emission of the photons. The band systems are defined according to the electronic transitions responsible for the near-ultraviolet (NUV) emission. The most intensive band systems are: Herzberg I, Herzberg II, Herzberg III, and Chamberlain system with the wavelength range 250–500 nm and the maximum of production at altitude ∼ 90–100 km above sea level [6].

To measure the absolute intensity of the NSB with respect to the dynamics of the airglow, we have developed an instrument AMON (Airglow MONitor). It is designed to be undemanding to power consumption and data rate, resistant to the whether conditions, and to have low construction and operation expenses. All these features allow to locate AMON instrument on different observational sites and provide simultaneous measurements of the NSB absolute intensities essential for the fluorescence high energy astrophysics, and the measurements of the NUV airglow variations necessary for the aeronomy studies. The aim of this paper is to introduce the AMON instrument (Section 2), describe its calibration and data reduction (Section 3), and to present its initial operation and first data analysis (Section 4).

2. Description of AMON instrument

The AMON instrument is fully developed by the Department of Space Physics, Institute of Experimental Physics, Slovak Academy of Sciences. It is designed to be sensitive enough to detect the faint diffuse light of NSB, and to be easily operated and resistant to provide long term measurements from different observational sites. To fulfill these requirements the following components are employed.
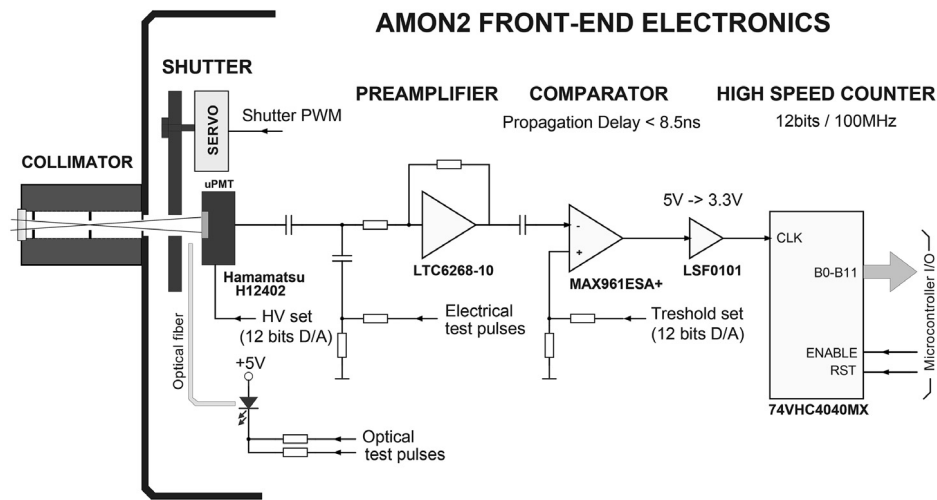

AMON2 FRONT-END ELECTRONICS

Fig. 1. The schematic view of the instrument front-end electronics. The main components are indicated with the exact denotations.

The light is measured by the tiny, thin and high-sensitivity photosensor-micro photomultiplier tube (μPMT) assembly H12402 manufactured by Hamamatsu [11]. The pixel of this one-pixel photosensor is represented by the bialkali photocathode with an effective area of 3×1 mm. The spectral response is 300–650 nm with a typical quantum efficiency of 26%, at the peak wavelength of 420 nm. The gain is $\sim 2 \times 10^6$ at the characteristic supply voltage of 900 V with the pulse rise time being 1.2 ns. The connected electronics work in the single photoelectron counting mode. The signal generated by the photosensor is amplified by the ultra-low bias current FET-input amplifier and subsequently discriminated by the threshold value of the analog discriminator. The pulses above the threshold value are counted by the high speed 12-stage binary counter. The schematic view of this front-end electronics is displayed in Fig. 1. The number of counts during exposure time with duration 1 s is processed by the low-power microcontroller and sent by the ethernet module via Internet to the server. The whole instrument is powered using the power over ethernet (PoE) technology. The power consumption is less than 1 W for the whole instrument.

Before the light reaches the photosensor, it is filtered by Thorlabs BG3 bandpass filter (FGB25S) [12], that has no anti-reflection coating. The transmission of the filter is higher than 50% in the wavelength ranges 315–445 nm and 720–1050 nm. The transmitted light is then collimated by a narrow collimator. The geometry of the AMON's collimator with the dimensions of the apertures is displayed in Fig. 2. The inner part of the collimator is made by chemically blackened copper (by potassium persulfate with sodium hydroxide bath), that provides anti-reflection and high-absorptive microcrystalline surface structure. The advantage of an imaging system using the collimator instead of lenses or mirrors are that the spectral uncertainties of the optics and the multiple reflections of the diffuse light in the optics are excluded. The instrument geometrical factor [13], that describes the ratio between the number of photons arriving at the detector's effective area and the number of photons emitted per unit area, and solid angle from an isotropic source located at an infinite distance, is 1.32×10^{-9} m^2 sr.

The AMON instrument is waterproof with a weight of 575 g and dimensions of $110 \times 75 \times 95$ mm (Fig. 3). The complementary sensors integrated in the instrument are lux-meter, thermometer, barometer, humidity-meter, GPS receiver, module of 3D accelerometer, gyroscope, and magnetometer. They provide continuous information which is important for AMON's safe operation. The lux-meter controls the opening of the shutter during sufficiently dark conditions to protect the highly sensitive μPMT sensor from the daylight. Thermometer, barometer, and humidity-meter measure the conditions inside the instrument to control the operation of thermo-regulation system that protect μPMT against very low temperatures. The GPS receiver provides time synchronization
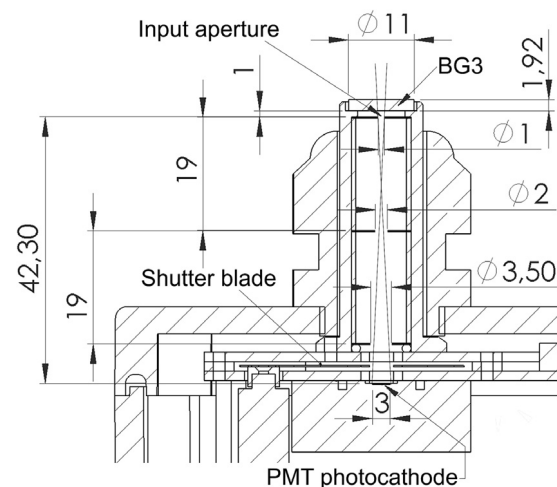

Fig. 2. The geometry and indication of the main parts of the instrument collimator. The dimensions are in the units of mm.

for all the acquired data and location information of the instrument. The module of 3D accelerometer, gyroscope, and magnetometer is employed to identify the instrument orientation in the three dimensional space.

All AMON data — scientific data, operational data, and housekeeping data are automatically transferred to the remote server in ASCII format. There, the data are parsed, stored in the database, and can be presented online through the web interface. The data transfer bandwidth is ~ 100 B/s. The instrument can be commanded remotely via the proprietary network protocol. Both actions — data monitoring and instrument commanding can be performed in real-time from any location with the Internet connection. The overall instrument electronics block scheme is displayed in Fig. 4. The main specifications of the AMON instrument are summarized in Table 1.

3. Calibration and data reduction

3.1. AMON laboratory calibration

The AMON instrument was calibrated in the laboratory conditions to obtain the absolute quantum efficiency of the μPMT. The method described in previous studies [14,15] was used for the calibration, because it provides confident absolute efficiency estimation with the systematic uncertainty less than 5%. The absolute efficiency was estimated for the
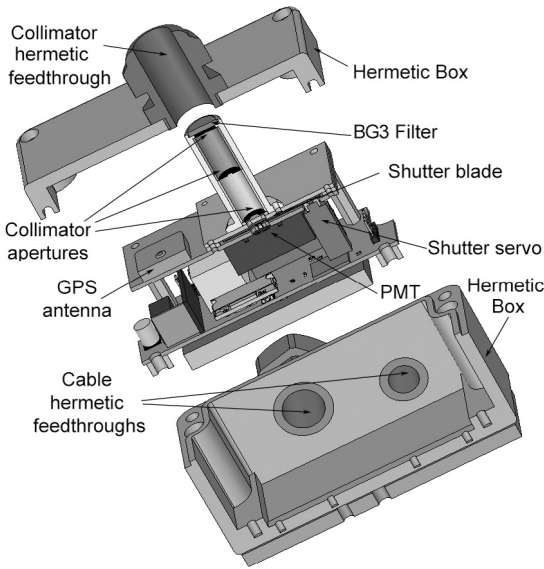
Fig. 3. The exploded view of instrument with the indication of the main components.
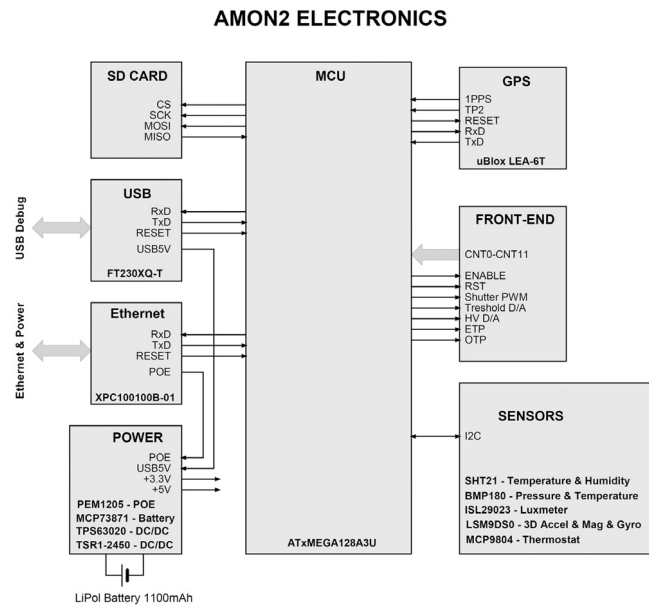
AMON2 ELECTRONICS

Fig. 4. The instrument's overall electronics block scheme. The main components are indicated with the exact denotations.

Table 1
The main specifications of the AMON instrument.

Parameter	Value
Dimensions	$110 \times 75 \times 95$ mm
Weight	575 g
Spectral range	300–480 nm
Integration time	1 s
Data rate	~100 B/s
Power consumption	~1 W
Light condition for operation	<0.3 lx
Ambient temperature range of operation	−20 to +50 °C

wavelength of 398 nm which is in the central position of the μPMT spectral characteristics. The relative quantum efficiency of the μPMT as a function of wavelength is well-defined by the manufacturer [11]. Before the calibration process, the μPMT high voltage was set to 950 V and the discriminator threshold, that discriminates noise from the single

photoelectrons, to 100 mV. These values were specified according to the measurements of the S-curve. The estimation of the photoelectrons pile-up effect was performed to ensure the linear response of the μPMT for the range of measured count rates. The pulse width of the discriminator output is 5.2 ns.

During the calibration, the AMON with unmounted collimator was attached to the port of an integrating sphere, while the light was produced by the LED with a wavelength of 398 nm attached to the second port of the integrating sphere. The intensity of the illumination was controlled by the NIST calibrated photodiode (OPHIR, PD300-UV [16]) attached to the third port. The light from the integrating sphere was collimated by two precise pinholes with an aperture diameter of 0.1 mm and the relative distance of 2 mm. The same optical axis for the calibrated μPMT and integrating sphere collimator was assured by the precise movement of the integrating sphere (with precision up to 10 μm) in the horizontal and vertical axis. By this set-up, the μPMT sensor inside the AMON instrument was receiving all the light coming from the integrating sphere through the collimator. The μPMT count rate and power received by NIST photodiode were recorded. Then, the AMON instrument was replaced by the second NIST photodiode and the LED light was increased, because the second NIST photodiode is less sensitive than the μPMT. By these measurements, the ratio between the intensity measured by the first and second NIST photodiode was obtained. Using this ratio we could calculate how many photons reached the μPMT per 1 s and compare this value with the recorded AMON count rate of single photoelectrons. This gave us absolute quantum efficiency of the μPMT which is 20.9% $\pm$ 1.1% for the wavelength of 398 nm. It is noteworthy that μPMT dark count rate is in the order of 10 Hz, which is negligible comparing to the count rate in the order of 0.1–1 MHz during the calibration.

The spectral characteristics of the BG3 bandpass filter transmittance is specified by the manufacturer [12]. The multiplication of relative efficiency of μPMT as the function of wavelength, that is normalized to the absolute efficiency at 398 nm, and the spectral transmission of the BG3 bandpass filter are displayed in Fig. 5. It is important to note that the atmospheric transmission introduces a cutoff at about 300 nm in real condition.

As it is mentioned in Section 2, the analytically calculated geometrical factor (GF) of the AMON's collimator used for calibration is 1.32×10^{-9} m^2 sr. This number represents the ratio between the collimator length (D), i.e., 42.3 mm and input area ($A_{entrance}$) with a diameter of 1 mm, multiplied by the effective area of μPMT ($A_{\mu PMT}$), i.e., 3×1 mm:

$$GF \simeq \frac{A_{\mu PMT} \, A_{entrance}}{D^2}. \tag{1}$$

To confirm the value of the GF, we have calculated AMON's field of view (FOV) by measurements of the duration while the NUV bright star is passing through the FOV (see Fig. 8). The measured FOV is consistent with the calculated solid angle from the GF within 10%. This includes uncertainty of the estimation of FOV by passing star method that is less than 5%. The uncertainty of the FOV estimation will be reduced in the future by precise measurements in the laboratory conditions.

The measured AMON count rate (R) that expresses number of counts per 1 second depends on the instrument's GF, total spectral efficiency ($\varepsilon_{\mu PMT}(\lambda) . T_{BG3}(\lambda)$) and measured diffuse source light ($\Phi(\lambda)$) at an infinite distance. This relation can be expressed by the following equation [17]:

$$R = GF \int_0^\infty \varepsilon_{\mu PMT}(\lambda) \, T_{BG3}(\lambda) \, \Phi(\lambda) \, d\lambda. \tag{2}$$

The AMON count rates can be then converted to the standard units used in high energy astrophysics, i.e., photons m^{-2} sr^{-1} ns^{-1} nm^{-1} by using Eq. (2), with the simplified assumption that the diffuse light of night sky background ($\langle NSB \rangle$) is not a function of the wavelength. Considering the conversion factor of the count rate from per seconds
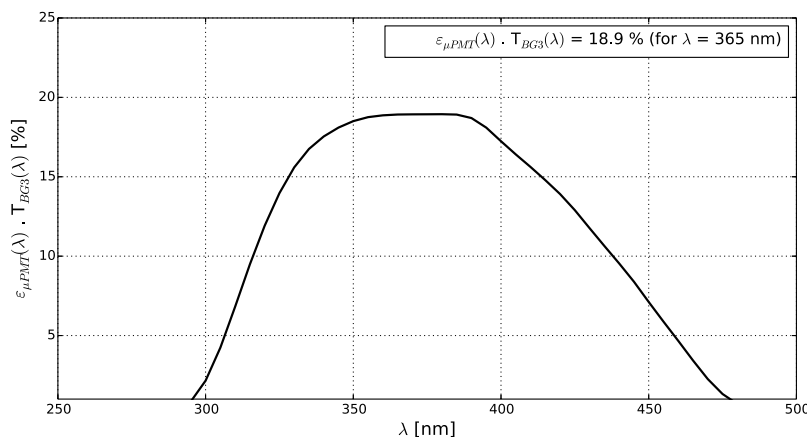
Fig. 5. The AMON's total spectral efficiency as the multiplication of the spectral characteristics of the calibrated μPMT (H12402) and BG3 bandpass filter (FGB25S).

to per nanoseconds ($\times 10^{-9}$), the searched value of $\langle NSB \rangle$ intensity can be expressed as:

$$\langle NSB \rangle = \frac{R \times 10^{-9}}{GF \int_0^\infty \varepsilon_{\mu PMT}(\lambda)\, T_{BG3}(\lambda)\, d\lambda}. \tag{3}$$

For example, by using Eq. (3) and taking into account the wavelength range of 300–480 nm, the value of 200 counts per second represents the NSB intensity of 1187 ± 178 photons m^{-2} sr^{-1} ns^{-1}. The total uncertainty involves the systematic uncertainty (up to 12%) and the statistical uncertainty that depends on the particular measurements. Usually, the total uncertainty is up to 15%.

It is important to note that the assumption of the constant NSB over the wavelength range was used due to approximately flat shape of the airglow spectrum in range 300–480 nm. This assumption introduces another systematic uncertainty to the estimation of NSB absolute intensity. To evaluate this particular systematic uncertainty, we have employed data from the high-resolution terrestrial night airglow emission line atlas [18,19]. The spectrum was normalized to unity in the wavelength range 300–480 nm, while the resolution was averaged within 1 nm and the missing values were interpolated. The effect of an atmospheric extinction was considered. The integral of AMON's total spectral efficiency and specified normalized spectrum in wavelength range 300–480 nm is 0.134. This leads to NSB intensity of 1130 photons m^{-2} sr^{-1} ns^{-1} by using count rate and GF from previous example. It means that the values of NSB absolute intensity differ in terms of 5% for assumption of constant NSB spectrum in comparison with the typical NSB spectrum. The topic of NSB spectrum shape and its influence on evaluation of the absolute intensities is widely discussed in the previous study [20].

3.2. AMON data reduction

The main condition for the NSB measurement analysis is the selection of the data based on the altitude of the sun and moon above the horizon. The AMON measurements are valuable only during the moonless astronomical nights, i.e., when the altitude of the sun is less than $-18°$ and the altitude of the moon is less than $0°$ above the horizon. The sensitivity of AMON with respect to the altitude of the sun and moon is plotted in Fig. 6. The altitude of the sun and moon above the horizon is calculated by using the PyEphem astronomy library for Python [21].

Another source of the contamination of AMON data is the presence of the bright astronomical objects in the FOV. The presence of the planets or the bright stars can be recognized and eliminated from the data easily. The star, which is passing the FOV, is represented as a sudden increase and decrease of the intensity (Fig. 6, at $\sim 20{:}40$ (UTC)). These light peaks could be removed by a simple method, by assuming Poisson distribution of NSB data. The square root of the mean value of the data from specific time interval is compared with the standard deviation of these data.

If the bright star is present, the standard deviation is higher than the square root of the mean value multiplied by a selected factor. The elimination of the effect of the groups of stars, as it is in the Milky Way galactic plane, is not so straightforward. This issue could be overcome by pointing the detector to a specific orientation towards the celestial pole. In this orientation, the contribution of the starlight is constant during the whole year. Also the contribution of the zodiacal light can be assumed constant for this orientation. The influence of the starlight and zodiacal light is widely discussed in some previous studies [3,22,23]. However, the orientation towards the celestial pole is not very convenient for the observational sites at the low latitudes. For them, the celestial pole is too close to the horizon, and so the atmospheric extinction is too high for NUV wavelengths.

All of the above mentioned conditions are predictable and the appropriate data for the analysis can be selected by well-defined rules. The selection process is not predictable for the weather conditions. The main weather condition that needs to be filtered out properly is the cloud coverage. The presence of clouds blocks the downwelling NUV radiation and can produce spurious variation of NSB. We use three types of approach to make a confident selection of the clear sky night hours — the simulated data of cloud coverage from the weather forecast service [24], the data from infra-red cloud sensor placed next to AMON during the measurements that were processed according to previous study [25], and the AMON data reduction based on the recognition of clear sky conditions in the data light curve. The detailed description of the methods for cloud coverage monitoring is out of the scope of this paper.

4. Initial operation and first data analysis

The AMON data are precious for the high-energy astrophysics and the aeronomy studies only after precise calibration and the data reduction when the sources of the data contamination are excluded, as it is described in Section 3. During the initial operation, the data were acquired from four AMON instruments operated at four observational sites (Fig. 7). The selection of the locations is based on a recent study [26]. The list of the observational sites with the position information is presented in Table 2.

For the purposes of high-energy astrophysics, we have analyzed the absolute intensities measured by AMON instruments. The measurements with the similar intent were also described by other researchers [17,27,28]. The AMON measurements during one night at LSO are displayed in Fig. 8. At this time, the AMON was pointing to the zenith. For the estimation of absolute intensity of NSB, the contribution from bright star is excluded. The average absolute intensity is 1016 photons m^{-2} sr^{-1} ns^{-1} with the total uncertainty of 15%. It is important to note that this value is only for this particular night and location. But in general, considering the wavelength range used and the airglow variations in time and location, this value is consistent with the results of other studies (Table 3).
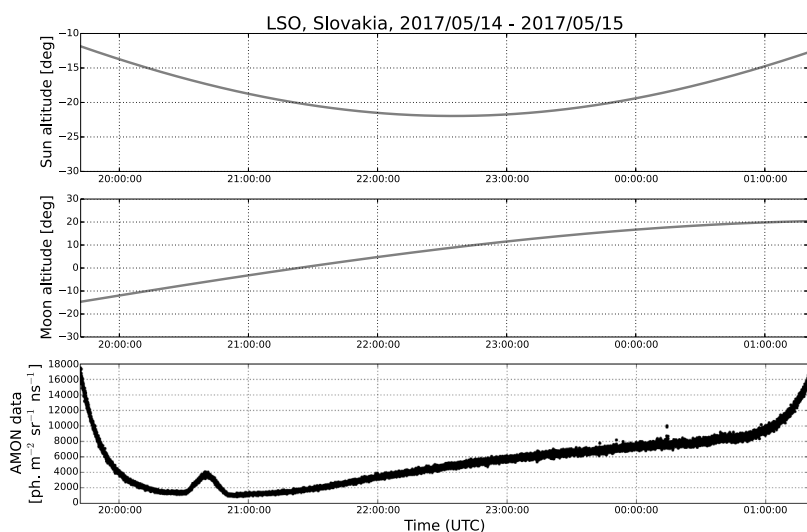
Fig. 6. Top: The altitude of the sun above the horizon for the location Lomnický Štít Observatory (LSO) in Slovakia and for the night of 14–15 May 2017. Middle: The altitude of the moon above the horizon for the same location and time. The period is 18 days after the new moon. Bottom: The measurements of the AMON instrument located at LSO. The astronomical night is during that period when the sun altitude is less than −18° and the moonless night time is during the period when the moon altitude is less than 0°. The peak at ~ 20:40 is caused by the contribution from the star Alkaid (η UMa, spectral type B4V).
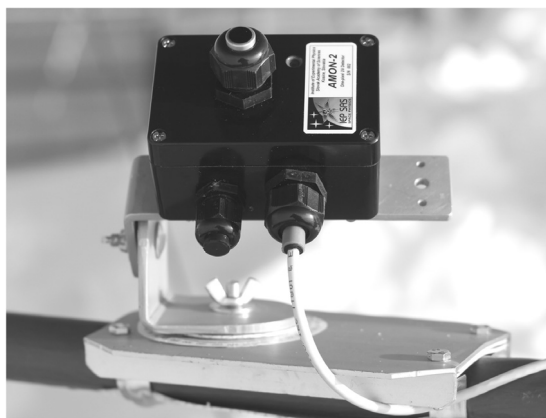
Fig. 7. The AMON instrument at Lomnický Štít Observatory, Slovakia (LSO) in May 2017.

Table 2
The locations of the AMON instruments during the initial operation in Spring 2017–Spring 2018.

Observational site	Acronym	Latitude [deg]	Longitude [deg]	Altitude [m a.s.l.]
Lomnický Štít Obs. (Slovakia)	LSO	49.19	20.21	2634
National Astronomical Obs. San Pedro Martir (Mexico)	OAN	31.05	−115.46	2788
El Roque de Los Muchachos Obs. La Palma (Spain)	ORM	28.76	−17.89	2167
Karby, Stockholm (Sweden)	STO	59.55	18.20	29

The airglow is a dynamic phenomenon and it introduces different variations to the NSB measurements. The variation of the absolute intensities, averaged per two hours for fourteen consecutive moonless nights with clear sky conditions, are presented in Fig. 9. Only the data from 04:00 to 06:00 (UTC) for each night were used to ensure similar influence of the astronomical objects. The data are presented in the relative units (r.u.) to emphasize the scale of variation. This type of measurements could be useful for the purposes of the aeronomy studies, because it indicates the presence of disturbances in the Earth's upper atmosphere. During the nights of 20–24 December 2017, the measurements

Table 3
The night sky background measurements. The details of measurements and their uncertainties are described in the particular references. It is important to note that NSB is not constant at all and the values of NSB are listed for the purpose to express the level of consistency of various measurements.

Reference	Location	Time	Wvl. range [nm]	NSB [ph. m^{-2} sr^{-1} ns^{-1}]
[27]	Canary Islands	May 2000	300–650	~2500
[27]	Namibia	June 2000	300–650	~2200
[28]	NSW, Australia	August 2010	300–650	~2000
[17]	Argentina	April 2010	300–430	~800
[17]	Argentina	April 2010	410–430	~200
AMON (Fig. 8)	Slovakia	April 2017	300–480	~1000

reflect unchanging conditions of airglow radiation. However, the measurements before and after this period indicate noticeable changes in the measured intensities. According to the detailed inspection of the weather conditions for these nights, the observed noticeable variations were not caused by the presence of clouds. So the possible interpretation is that the observed airglow layer was disturbed during nights of 18–19 December and 24–25 December. Such disturbances could cause the variation of density of molecular oxygen (O_2), which is responsible for airglow light production in NUV range.

By using the network of AMON instruments (AMON-net), it might be possible to measure the evolution of airglow variations in time and space, and to contribute to the better understanding of these phenomena. More comprehensive data analyses from all four AMON instruments is ongoing and it is planned to be published in a separate paper.

5. Conclusions

The AMON instrument is the one-pixel detector for airglow monitoring in the near-ultraviolet spectral band. It is designed to provide valuable information of the night sky background (NSB) required for the high-energy astrophysics fluorescence telescopes. The AMON instrument could produce useful information also for the aeronomy and contribute to the understanding of the night airglow composed by the emission of molecular oxygen.

In this study, we have described the details of the AMON's construction together with the characterization of its subsystems. The process of the laboratory calibration is reported and the total efficiency of the instrument is evaluated. The AMON operation in the real conditions
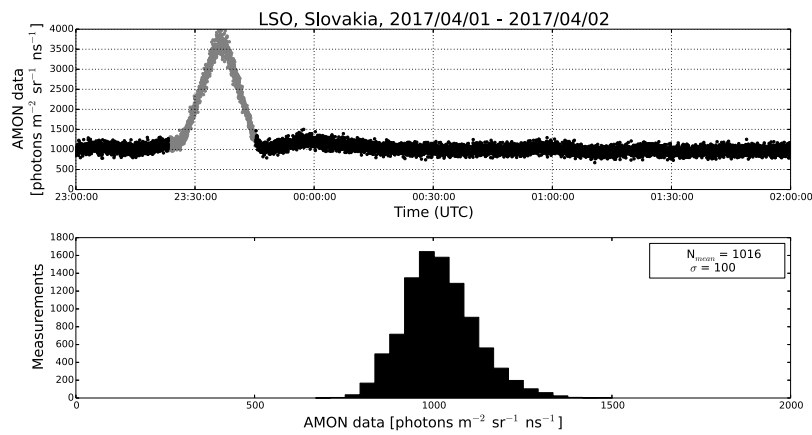
Fig. 8. TOP: The AMON measurements during the night of 1–2 April 2017 at LSO. The data used for the estimation of absolute intensity are marked with black dots. The peak, marked with gray dots, represents the star Alkaid (η UMa, spectral type B4V) in the AMON's FOV and they are excluded from the absolute intensity estimation by automated method described in Section 3.2. Bottom: The distribution of AMON measurements with bin size 20 photons m^{-2} sr^{-1} ns^{-1}. The average intensity with standard deviation are indicated in the top right label.
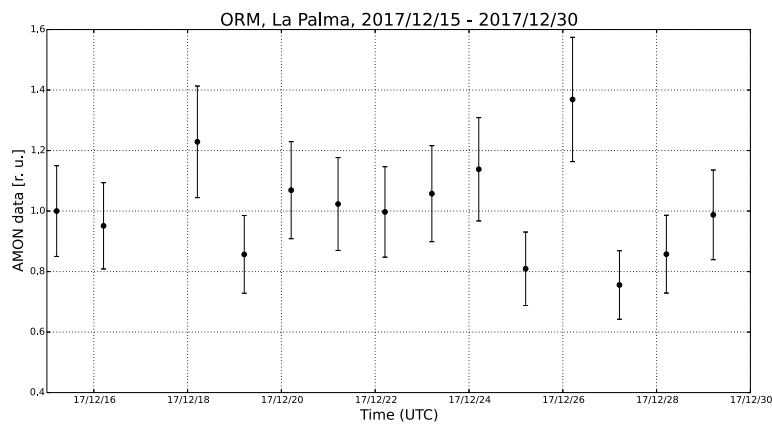
Fig. 9. The AMON measurements during the nights of 15–30 December 2017 at ORM. The data from the night of 16–17 December are not displayed because the clear-sky conditions were not fulfilled for this night. The same filter for the star contamination reduction is used, as presented in Fig. 8. Each of the point represents the average value per two hours of measurements from 04:00 to 06:00 (UTC). The average values are displayed in relative units with respect to the value of the first point. The size of error-bars is 15% and represents the total uncertainty of the particular average value.

is presented, while the data reduction was applied. The examples of the first data indicates the usefulness of the AMON for the intended purposes. The detailed data analysis is ongoing and the extension and operation of the fully automated network of AMON instruments (AMON-net) is planned for the future.

References

[1] S.M. Silverman, Night airglow phenomenology, *Space Sci. Rev.* 11 (1970) 341–379.

[2] R.R. Meier, Ultraviolet spectroscopy and remote sensing of the upper atmosphere, *Space Sci. Rev.* 58 (1991) 1–185.

[3] C. Leinert, S. Bowyer, L.K. Haikala, M.S. Hanner, M.G. Hauser, A.-C. Levasseur-Regourd, I. Mann, K. Mattila, W.T. Reach, W. Schlosser, H.J. Staude, G.N. Toller, J.L. Weiland, J.L. Weinberg, A.N. Witt, The 1997 reference of diffuse night sky brightness, *Astron. Astrophys. Suppl.* 127 (1998) 1–99.

[4] K.A. Deutsch, G. Hernandez, Long-term behavior of the OI 558 nm emission in the night sky and its aeronomical implications, J. Geophys. Res. (Space Phys.) 108 (2003) 1430.

[5] I.M. Reid, A.J. Spargo, J.M. Woithe, Seasonal variations of the nighttime O (1S) and OH (8-3) airglow intensity at Adelaide, Australia, J. Geophys. Res.: Atmos. 119 (11) (2014) 6991–7013.

[6] V.Y. Khomich, A.I. Semenov, N.N. Shefov, Airglow as an Indicator of Upper Atmospheric Structure and Dynamics, Springer-Verlag, 2008.

[7] R.F. Pfaff, The near-earth plasma environment, *Space Sci. Rev.* 168 (2012) 23–112.

[8] J.H. Adams, S. Ahmad, J.-N. Albert, D. Allard, M. Ambrosio, L. Anchordoqui, A. Anzalone, Y. Arai, C. Aramo, K. Asano, et al., An evaluation of the exposure in nadir observation of the JEM-EUSO mission, Astropart. Phys. 44 (2013) 76–90.

[9] K. Louedec, A tmospheric effects in astroparticle physics experiments and the challenge of ever greater precision in measurements, Astropart. Phys. 60 (2015) 54–71.

[10] B. Keilhauer, M. Bohacova, M. Fraga, J. Matthews, N. Sakaki, Y. Tameda, Y. Tsunesada, A. Ulrich, Nitrogen fluorescence in air for observing extensive air showers, in: European Physical Journal Web of Conferences (2013), Vol. 53, 2013, p. 01010.

[11] Hamamatsu, MICRO PMT ASSEMBLY H12402, available at, https://www.hamamatsu.com/resources/pdf/etd/MicroPMT_TPMZ1019E.pdf (accessed 16.10.18).

[12] Thorlabs, BG3 Colored Glass Bandpass Filter, 315 - 445 nm, available at, https://www.thorlabs.com/thorproduct.cfm?partnumber=FGB25S (accessed 16.10.18).

[13] J.D. Sullivan, Geometrical factor and directional response of single and multi-element particle telescopes, Nucl. Instrum. Methods 95 (1971) 5.

[14] C. Blaksley, P. Gorodetzky, A setup for the precision measurement of multianode photomultiplier efficiency, Nucl. Instrum. Methods Phys. Res. A 764 (2014) 198–205.

[15] J.H. Adams, S. Ahmad, J.-N. Albert, D. Allard, L. Anchordoqui, V. Andreev, A. Anzalone, Y. Arai, K. Asano, M. Ave Pernas, et al., Calibration aspects of the JEM-EUSO mission, Exp. Astron. 40 (2015) 91–116.

[16] Ophir, PD300-UV, Standard Photodiode Sensor, available at, https://www.ophiropt.com/laser--measurement/sites/default/files/PD300-UV_PD300-UV-193_PD300-IR_PD300-IRG_1.pdf (accessed 16.10.18).

[17] M.C. Maccarone, O. Catalano, S. Giarrusso, G. La Rosa, A. Segreto, G. Agnetta, B. Biondo, A. Mangano, F. Russo, S. Billotta, Performance and applications of the UVscope instrument, Nucl. Instrum. Methods Phys. Res. A 659 (2011) 569–578.

[18] R.W. Hanuschik, A flux-calibrated, high-resolution atlas of optical sky emission from UVES, *Astron. Astrophys.* 407 (2003) 1157–1164.

[19] P.C. Cosby, B.D. Sharpee, T.G. Slanger, D.L. Huestis, R.W. Hanuschik, High-resolution terrestrial nightglow emission line atlas from UVES/VLT: Positions, intensities, and identifications for 2808 lines at 314-1043 nm, J. Geophys. Res. (Space Phys.) 111 (A10) (2006) A12307.

[20] JEM-EUSO collaboration, G. Abdellaoui, S. Abe, J.H. Adams Jr, et al., Ultra-violet imaging of the night-time earth by EUSO-Balloon towards space-based ultra-high energy cosmic ray observations, Astropart. Phys. (2018) http://dx.doi.org/10.1016/j.astropartphys.2018.10.008, (in press).

[21] PyEphem, astronomy library for Python, available at, http://rhodesmill.org/pyephem/ (accessed 16.10.18).

[22] R.A. Bernstein, W.L. Freedman, B.F. Madore, The first detections of the extragalactic background light at 3000, 5500, and 8000 Å. II. Measurement of foreground zodiacal light, *Astrophys. J.* 571 (2002) 85–106.

[23] S. Noll, W. Kausch, M. Barden, A.M. Jones, C. Szyszka, S. Kimeswenger, J. Vinther, A n atmospheric radiation model for Cerro Paranal. I. The optical spectral range, *Astron. Astrophys.* 543 (2012) A92.

[24] Meteoblue, Historical weather data, available at, https://content.meteoblue.com/tr/sectors/science (accessed 16.10.18).

[25] M.-H. Ahn, D. Han, H.-Y. Won, V. Morris, A cloud detection algorithm using the downwelling infrared radiance measured by an infrared pyrometer of the ground-based microwave radiometer, Atmos. Meas. Tech. Discuss. 7 (2014) 9413–9452.

[26] M. Putis, P. Bobik, S. Mackovjak, M ethod for analysis of the effect of geomagnetic disturbances on UV airglow intensity, Earth Space Sci. 5 (11) (2018) 790–800.

[27] S. Preuss, G. Hermann, W. Hofmann, A. Kohnle, Study of the photon flux from the night sky at La Palma and Namibia, in the wavelength region relevant for imaging atmospheric Cherenkov telescopes, Nucl. Instrum. Methods Phys. Res. A 481 (2002) 229–240.

[28] D. Hampf, G. Rowell, N. Wild, T. Sudholz, D. Horns, M. Tluczykont, Measurement of night sky brightness in southern Australia, Adv. Space Res. 48 (2011) 1017–1025.